

Lapse-time-dependent coda-wave depth sensitivity to local velocity perturbations in 3-D heterogeneous elastic media

Anne Obermann,¹ Thomas Planès,² Céline Hadziioannou³ and Michel Campillo⁴

¹Swiss Seismological Service, ETH Zurich, Zurich, Switzerland. E-mail: anne.obermann@sed.ethz.ch

²Department of Geophysics, Colorado School of Mines, Golden, CO, USA

³Department of Earth and Environmental Sciences, Ludwig-Maximilians-Universität, Munich, Germany

⁴ISTerre, Université de Grenoble, Grenoble, France

Accepted 2016 July 14. Received 2016 May 25; in original form 2016 January 11

SUMMARY

In the context of seismic monitoring, recent studies made successful use of seismic coda waves to locate medium changes on the horizontal plane. Locating the depth of the changes, however, remains a challenge. In this paper, we use 3-D wavefield simulations to address two problems: first, we evaluate the contribution of surface- and body-wave sensitivity to a change at depth. We introduce a thin layer with a perturbed velocity at different depths and measure the apparent relative velocity changes due to this layer at different times in the coda and for different degrees of heterogeneity of the model. We show that the depth sensitivity can be modelled as a linear combination of body- and surface-wave sensitivity. The lapse-time-dependent sensitivity ratio of body waves and surface waves can be used to build 3-D sensitivity kernels for imaging purposes. Second, we compare the lapse-time behaviour in the presence of a perturbation in horizontal and vertical slabs to address, for instance, the origin of the velocity changes detected after large earthquakes.

Key words: Interferometry; Seismic monitoring and test-ban treaty verification; Body waves; Surface waves and free oscillations; Coda waves; Wave scattering and diffraction.

1 INTRODUCTION

Changes in the seismic waveform between two perfectly reproducible acquisitions can be attributed to variations of elastic properties in the evolving medium (Reasenber & Aki 1974). In mainly homogeneous lithologies, strong medium changes might be detected by direct waves, however, their sensitivity to weak changes is low. The seismic coda, the product of multiple scattering processes caused by heterogeneities in the Earth (Aki 1969), on the other hand, samples the propagation medium very densely and for a long time, resulting in a high sensitivity to tiny modifications of the seismic properties in the medium (e.g. Poupinet *et al.* 1984, 1996; Snieder *et al.* 2002). This sensitivity has been successfully used for monitoring purposes in different areas of seismology, recently using ambient noise cross-correlations [e.g. volcanoes (Sens-Schönfelder & Wegler 2006), fault zones (Brenquier *et al.* 2008), engineering projects (Hillers *et al.* 2015; Salvermoser *et al.* 2015)]. In these applications the detected waveform change is a traveltimes delay that can be linked with changes in the mechanical properties of the propagating medium. The distortion of the waveform (or decorrelation) is another type of observation that is linked to changes in the scattering properties of the medium (Larose *et al.* 2010).

Besides the detection of medium changes, a central question is their location. Depending on the position of the sensors relative to the spatially inhomogeneous change, lateral variations in the ampli-

tude of the waveform changes are observed (e.g. Chen *et al.* 2010; Sens-Schönfelder & Wegler 2011) that can be used for 2-D mapping purposes. Brenquier *et al.* (2008) attributed the velocity changes to ellipses area around each station pair; Hobiger *et al.* (2012) assigned the velocity changes directly to the station locations. Pacheco & Snieder (2005) developed probabilistic-based sensitivity kernels that describe the diffusive propagation of multiply-scattered waves and relate the effect of local velocity changes to phase-shifts in the coda waveforms. These probabilistic sensitivity kernels are calculated from the 2-D analytical solution of the diffusion equation. Their use in seismology is based on the assumption that coda waves are dominated by surface waves (2-D wave propagation). For greater insight into the links and differences between these kernels in different propagation regimes, the reader is referred to the work of Planès *et al.* (2014) and Margerin *et al.* (2016). Numerous studies have exploited 2-D versions of these sensitivity kernels to locate changes in the medium (Obermann *et al.* 2013a, 2014, 2015; Hillers *et al.* 2015; Planès *et al.* 2015). A mapping procedure using these sensitivity kernels can yield a lateral view on the medium changes. However, the depth of the changes remains a challenge.

Rivet *et al.* (2011) and Froment *et al.* (2013) studied waveform changes at great depth relying on the frequency dependent depth sensitivity of surface waves that they assume to dominate the coda waves based on diffuse wave theory (Hennino *et al.* 2001). Sens-Schönfelder & Wegler (2006) linked waveform changes at Merapi

volcano to changes in the hydrological system. Supported by the lapse time dependence of the waveform changes, they assume that the coda on the volcano is made up of scattered body waves rather than surface waves that show slower decay of sensitivity with depth. Larose *et al.* (2010, 2015) and Zhang *et al.* (2016) used a 3-D analytical solution of the diffusion equation to create probabilistic kernels that describe the volumetric body-wave propagation. These kernels were successfully used to monitor the crack evolution in a concrete block, a highly heterogeneous medium where the ultrasonic coda is dominated by body waves.

In most crustal-like materials, the coda is actually a mixture of body and surface waves. Obermann *et al.* (2013b) have shown with wavefield simulations in a 2-D half-space with small-scale random heterogeneities that the relative contributions of surface waves and body waves to the coda sensitivity can be expressed as a partition ratio. This ratio essentially depends on the heterogeneity of the medium and the lapse-time in the coda. To accurately locate changes at depth, we hence need 3-D sensitivity kernels that take both surface and body waves into account. There is no analytical solution of the diffusion or radiative transfer theory in the half-space that takes mode conversions into account. At least two approaches could be followed to build these kernels. Kanu & Snieder (2015) numerically computed the intensity propagation of wavefields in 2-D (which includes mode conversions) and obtained sensitivity kernels after ensemble averaging over different medium realizations. This approach is particularly interesting in specific cases where deterministic structures in the medium dominate the wavefield properties. Extended to 3-D, this approach could yield accurate 3-D kernels that include all different modes of wave-propagation when a specific large-scale model is known. A second approach is to extend the analysis of Obermann *et al.* (2013b) to 3-D and evaluate the partition coefficient between body and surface waves. This will not yield the exact kernels as in a fully numerical approach, but based on partition coefficients adapted to the lapse time, this analysis allows for an approximate solution using a combination of the analytical kernels for surface waves (2-D) and body waves (3-D). This approach is a simple way to build 3-D kernels without explicitly modelling theoretically or numerically the mode conversions. The extension of the 2-D results of Obermann *et al.* (2013b) to 3-D might appear trivial, but it is essential, as the dimensionality is known to be of crucial importance for the behaviour of diffuse waves. While the construction of the sensitivity kernel for multiply scattered waves has been thoroughly revisited by Margerin *et al.* (2016) in 2-D media, one must notice that even the apparently simple problem of

the radiative transfer in 3-D for elastic waves in a half-space is still without formal solution.

In this paper, we restrain our analysis to velocity changes. After a description of the 3-D elastic heterogeneous medium in Section 2, we show in Section 3 that the depth sensitivity can be modelled as a combination of body and surface-wave sensitivities. We compute partition ratios of body and surface-wave sensitivities for media with different degrees of heterogeneity and at different lapse times in the coda. These partition ratios allow the construction of probabilistic 3-D sensitivity kernels for imaging purposes that combine surface and body wave propagation. In Section 4, we investigate the lapse time behaviour of the relative velocity changes and the correlation coefficients for different configurations of medium changes, to study, for instance, the origin of the velocity changes detected after large earthquakes.

2 NUMERICAL SIMULATIONS

To study the sensitivity of coda waves to velocity perturbations within a 3-D medium, we perform numerical simulations of wavefield propagation in a 3-D heterogeneous elastic medium without intrinsic attenuation. We use SPEC-FEM3D for the simulations, which is based on a continuous Galerkin spectral-element method (Komatitsch & Tromp 2002; Peter *et al.* 2011).

2.1 Model setup

The model size is $10 \times 10 \times 6$ km³ in the x -, y - and z -directions, respectively. The grid spacing is $\delta x = \delta y = \delta z = 50$ m. We record the wavefield for 16 s with a time step of 10^{-4} s. For the heterogeneous medium, we use a von-Karman distribution with a Hurst exponent of 0.5 and a correlation length of $a = 300$ m, which is of the order of the wavelength to enhance scattering. We consider different standard deviations in velocity fluctuations σ in the range of 10–50 per cent around a background P -wave velocity of $v_P = 6500$ m s⁻¹. The S -wave velocity depends on the P -wave velocity with $v_S = v_P/\sqrt{3}$. In this initial background velocity model, we introduce a small velocity reduction of $dv = 100$ m s⁻¹ ($\frac{dv}{v} \approx -1.54$ per cent) within a thin layer (100 m) at depth d (perturbed model). An isotropic source with a central frequency of 20 Hz is placed at $(x, y) = 5$ km in the first grid point below the surface ($z = 50$ m). Receivers are placed in a regular grid on the free surface with 0.5 km spacing. An example of this setup is shown in Fig. 1(a), with selected receivers. In Fig. 1(b) we show an example of a synthetic seismogram at 3 km distance

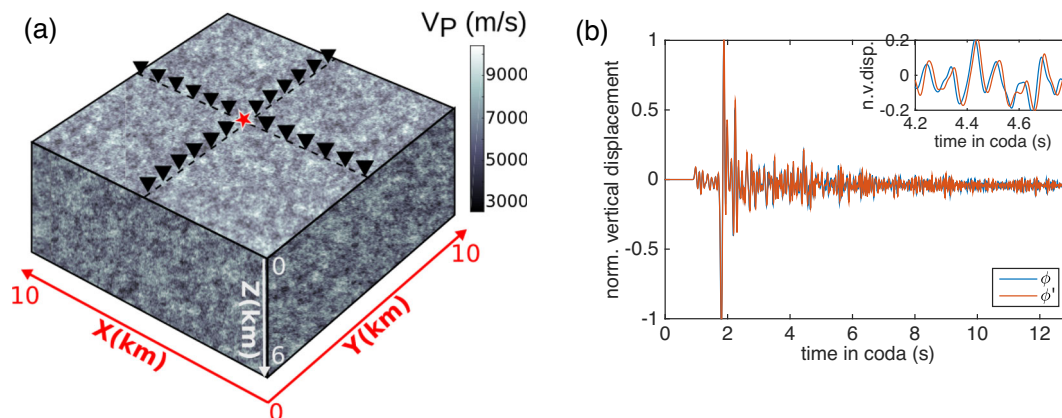


Figure 1. (a) Heterogeneous model $(x, y) = 10$ km, $z = 6$ km. The red star marks the source position and the black inverted triangles mark some exemplary receiver positions. (b) Synthetic seismograms recorded without (ϕ , blue) and with perturbed layer (ϕ' , red) at the surface in a medium with 20 per cent velocity fluctuation.

Table 1. Theoretical energy ratios in a Poisson half-space considering different types of waves measured at the surface ($z = 0$) and for an infinite medium ($z = \infty$), after Hennino *et al.* (2001) and Trégourès *et al.* (2002).

Type of waves considered	Depth	Theoretical energy ratio $\langle S^2 \rangle / \langle P^2 \rangle$
Only Rayleigh waves	$z = 0$	6.46
Only Body waves	$z = 0$	9.76
Mode conversions of Rayleigh and Body waves	$z = 0$	7.19
Mode conversions of Rayleigh and Body waves	$z = \infty$	10.39

from the source with (red) and without (blue) perturbed layer at the surface ($d = 0$ km).

As imperfect boundaries with different absorption characteristics for body and surface waves could alter the interpretation of our results at late lapse times, we tested the boundary conditions with the help of a homogeneous half-space. We placed a source and a receiver line at 1 km depth within the medium and studied the resulting reflections. We could only observe reflections due to the free surface and are hence confident that the boundaries are good enough for this study (see Fig. S1, Supporting Information).

2.2 Scattering characterization

2.2.1 Is the energy equipartitioned?

One of the characteristics of multiple scattering regimes is the partition of the energy of the different states of P and S waves in the coda (Weaver 1982, 1985). This partition ratio is defined by the propagating modes and is independent of the source types. In Table 1 we give the theoretical energy ratios $\langle S^2 \rangle / \langle P^2 \rangle$ in a Poisson half-space measured at the surface and at depth for different types of waves (Hennino *et al.* 2001; Trégourès *et al.* 2002). Hennino *et al.* (2001) and Margerin *et al.* (2009) studied the coda of earthquakes and could confirm the theoretical energy ratio for a half-space with homogeneous or stratified background.

To study the energy ratio in the numerical model, we place a source at $x, y = 5$ km, close to the free surface ($z = 50$ m). We arrange 60 receivers in 4 orthogonal lines in the medium ($z = 0.05:0.1:6$ km) at 3 km horizontal distance from the source. At each of the receivers we compute the spatial derivatives of the wavefield. We then calculate the energy ratio between the squared curl (S waves) and the squared divergence (P waves) of the wavefield in a sliding time-window of 3 s in the coda following Shapiro *et al.* (2000). These simulations are repeated 10 times for different realizations of the heterogeneous medium with the same statistical properties.

We observe a stabilization of the energy from about 3 to 25 s (Fig. 2b). In Fig. 2(a) we plot the $\langle S^2 \rangle / \langle P^2 \rangle$ -ratio with depth. Averaged over all receivers at various depths and models, we obtain an average ratio of $\langle S^2 \rangle / \langle P^2 \rangle = 9 \pm 2$. The ratio decreases close to the free surface as expected from the theory (7.2). At large depth, that is in the absence of Rayleigh waves, the $\langle S^2 \rangle / \langle P^2 \rangle$ -ratio is expected to be the one of the elastic Poissonian space (10.39). Our measurements show large fluctuations as seen on actual measurements on earthquake records (e.g. Margerin *et al.* 2009; Chaput *et al.* 2015). The analytical solution of Hennino *et al.* (2001), based on equipartition in a reference model that is without disorder, also show fluctuations due to interferences between upgoing and surface reflected waves. The fluctuations from one realization to the other, and from one depth to the other, are therefore not a surprise. Furthermore, the finite region of scattering in our computations implies

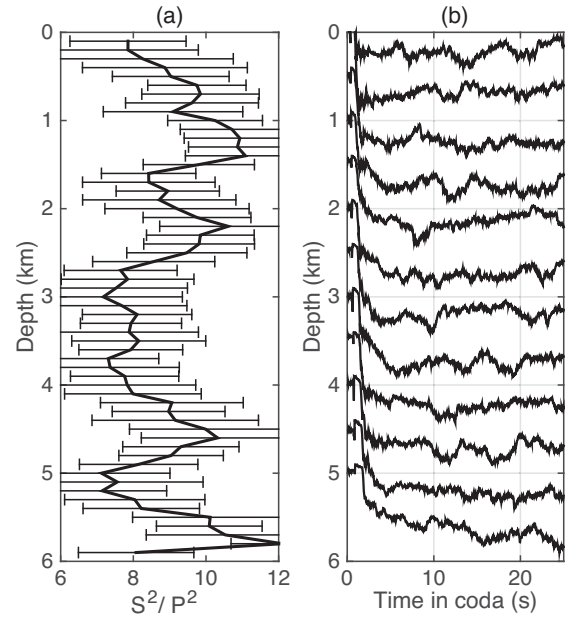


Figure 2. (a) Energy stabilization ratio $\langle S^2 \rangle / \langle P^2 \rangle$ at different depths averaged over 10 medium realizations. (b) Exemplary energy stabilization ratio $\langle S^2 \rangle / \langle P^2 \rangle$ of one realization with time in the coda for selected depth positions. The amplitude is normalized.

a leakage of energy at the boundaries that represents a further difference with the full space theoretical results. We use the ratio of 9/1 to calculate the energy velocity c_E for our study as:

$$\frac{1}{c_E} = \frac{0.89}{V_S} + \frac{0.11}{V_P}. \quad (1)$$

The energy velocity c_E is needed in the next section for the determination of the scattering mean free path. As a consequence of the energy partitioning the source characteristics can be neglected in our analysis.

2.2.2 Determination of the scattering mean free path

We determine the scattering mean free path ℓ and transport mean free path ℓ^* of the media from the coherent and incoherent parts of the recorded signals in a process similar to the one described in Obermann *et al.* (2013b). The different wavelengths of P and S waves cause a different sampling of the scattering pattern and result in different mean free paths for P and S waves. Here, we do not separate both wave-types, but rather consider the scattering mean free path for the wavefield as a whole. Thus, we measure an effective ℓ , which is associated with the propagation speed of the energy of the mixture of the P and S waves (c_E). For field data the degree of heterogeneity can often be estimated for instance via the decay of the coda envelope (Margerin *et al.* 1999; Nakahara &

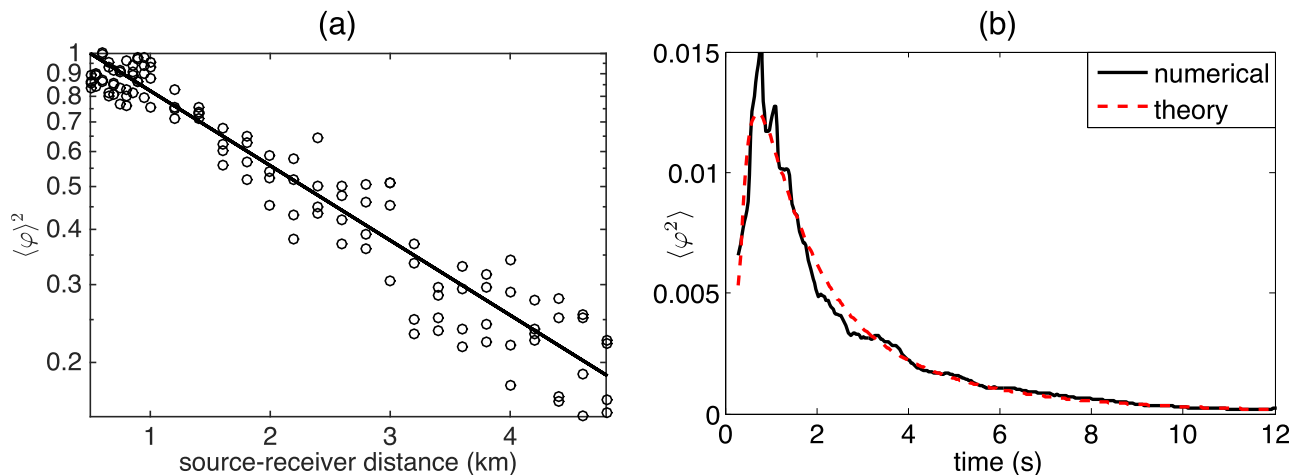


Figure 3. (a) Logarithm of the normalized coherent intensity $\langle \varphi \rangle^2$ versus source–receiver distance averaged over 10 simulations for models with $\sigma = 20$ per cent. After correcting for geometrical spreading, the slope is proportional to $-1/\ell$. (b) Normalized incoherent intensity $\langle \varphi^2 \rangle$ versus time. ℓ^* is calculated from the diffusion constant of the diffusion equation that gives the best fit.

Carcolé 2010), phase statistics (Obermann *et al.* 2014), or stochastic medium characterization (Nakata & Beroza 2015).

For these simulations, we use reflecting boundaries at all sides, place the source in the centre of the medium ($x, y = 5$ km, $z = 3$ km) and arrange 216 receivers in 3 orthogonal lines around the source ($x_1 = 0.05:0.05:10$ km, $y_1 = 5$ km, $z_1 = 3$ km; $x_2 = 5$ km, $y_2 = 0.05:0.05:10$ km, $z_2 = 3$ km; $x_3 = 5$ km, $y_3 = 5$ km, $z_3 = 0.05:0.05:5$ km). We correct the signals for 3-D geometrical spreading and plot the logarithm of the normalized coherent energy versus the source–receiver distance in Fig. 3(a). The slope of the regression line yields the scattering mean free path through $-1/\ell$. In Fig. 3(b), we plot the intensity and its best fit with the diffusion equation, which gives us an estimate of the transport mean free path $\ell^* = \frac{3D}{c_E}$, where D is the diffusion constant. The results in Fig. 3 are shown for models with $\sigma = 20$ per cent. In Table 2 we report the results for ℓ and ℓ^* for media with different degrees of heterogeneity (σ) with standard deviation, averaged over 10 model realizations each. The ratio between ℓ and ℓ^* is related to the degree of anisotropy of scattering. The anisotropy is governed by the ratio between the correlation length and the wavelength. In our case this ratio is close to 1 and anisotropic scattering is expected (e.g. Sato *et al.* 2002). As predicted by the theory, the ratio of ℓ and ℓ^* is stable (≈ 1.3) for different amplitudes of the fluctuations of σ .

The scattering properties of surface and body waves are likely to be different. We tested whether this has an effect on the determination of the scattering mean free path by comparing our results with the coda decay in a heterogeneous full-space. We could not observe any significant systematic differences for the tested cases. Please note, that a frequency dependence of the results is taken into account through the velocity of the surface waves and the mean free path.

Table 2. Transport and Scattering mean free path calculated numerically for models with different amounts of heterogeneity.

Model	Transport mean free path (ℓ^*)	Scattering mean free path (ℓ)
$\sigma = 10$ per cent	2620 m \pm 6 per cent	2000 \pm 6 per cent
$\sigma = 20$ per cent	1840 m \pm 5 per cent	1370 \pm 5 per cent
$\sigma = 30$ per cent	1220 m \pm 5 per cent	1000 \pm 5 per cent
$\sigma = 40$ per cent	880 m \pm 2 per cent	700 \pm 3 per cent
$\sigma = 50$ per cent	650 m \pm 2 per cent	500 \pm 3 per cent

3 MODELLING RELATIVE VELOCITY CHANGES WITH DEPTH

3.1 Apparent relative velocity changes with depth

We use the stretching method (Lobkis & Weaver 2003; Sens-Schönfelder & Wegler 2006; Hadziioannou *et al.* 2009) to determine the apparent relative velocity changes ϵ^{obs} caused by the perturbed layer at each depth position. In Fig. 4, we plot the relative velocity changes versus depth for a medium with $\sigma = 20$ per cent at $t = 2$ s. We observe that the relative velocity change decreases with depth of the perturbed layer. We can discriminate two different regimes of sensitivity. In the first regime, for shallow layers (< 0.5 km), the sensitivity decays rapidly with depth, which we interpret as the signature of the depth sensitivity of the fundamental mode of the surface waves. In the second regime, which concerns deeper layers (> 0.5 km), the decay of sensitivity is much slower, which we interpret as an imprint of the 3-D diffusion of body

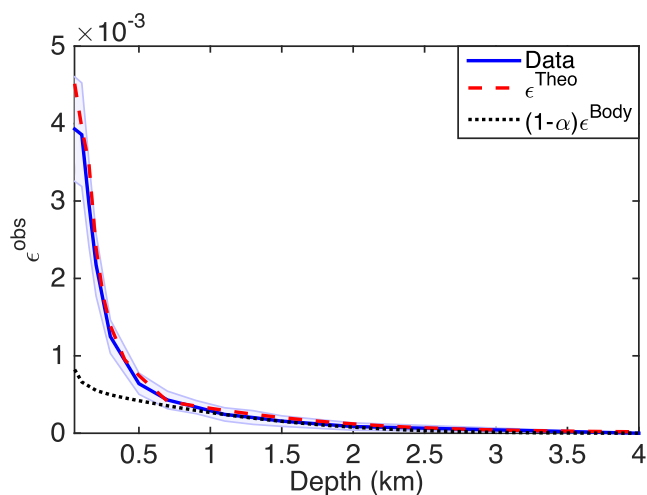


Figure 4. Apparent relative velocity changes with depth of the perturbed layer ($\sigma = 20$ per cent). The modelled data (dashed-red) $\epsilon^{\text{Theo}}(d, t = 2$ s) fit the observations very well. We note the importance of the surface waves, as the body-wave regime $(1 - \alpha)\epsilon^{\text{Body}}$ (with $\alpha = 0.75$) alone cannot account for the steep slope at short times.

waves. These observations are in agreement with the results from Obermann *et al.* (2013b) for the 2-D case.

3.2 Model for the depth sensitivity in the 3-D case

In the following we show that similarly to the 2-D case, in 3-D we can model the relative velocity changes $\varepsilon^{\text{Theo}}$ as a combination of body- and surface-wave sensitivities ($\varepsilon^{\text{Body}}$ and $\varepsilon^{\text{Surf}}$) according to:

$$\varepsilon^{\text{Theo}}(d, t) = \alpha(t)\varepsilon^{\text{Surf}}(d) + (1 - \alpha(t))\varepsilon^{\text{Body}}(d, t). \quad (2)$$

$\varepsilon^{\text{Body}}$ and $\varepsilon^{\text{Surf}}$ represent the apparent velocity variations of body and surface waves respectively. α is the fitting parameter that we refer to as partition coefficient. The sensitivity partition coefficient is different from the energy partition ratio, as it integrates the time the wave has spent in each state (surface or body wave). It is a non-trivial parameter that is also dependent upon the lag-time. In the following, we present a simple modelling based on the known properties of sensitivity of surface and body waves.

3.2.1 Surface wave sensitivity

Following Obermann *et al.* (2013b), we study the depth sensitivity of the surface waves $\varepsilon^{\text{Surf}}$ independent of body waves by considering propagating waves in a homogeneous 3-D medium. We introduce a thin layer with a slight velocity perturbation ($\frac{dv}{v} = 1.54$ per cent). The surface wave sensitivity decays rapidly and disappears after 700 m, which corresponds to a bit more than twice the central P-wavelength $\lambda_0 = 325$ m. The source is placed in the first grid point, which extends from 0-50 m, which could explain the differences in the sensitivity kernel compared to the study in 2-D, where the first grid point that contained the source extended from 0-20 m only, and where the surface wave sensitivity disappeared after $2/3 \lambda_0$. This sensitivity is similar to the one deduced from a perturbation analysis and is used in surface wave tomography (Aki & Richards 1980).

3.2.2 Body wave sensitivity

The contribution of the body wave sensitivity in the coda ($\varepsilon^{\text{Body}}$) is modelled with sensitivity kernel K introduced in Pacheco & Snieder (2005).

$$K(\mathbf{S}, \mathbf{R}, \mathbf{r}_0, t) = \frac{\int_0^t p(\mathbf{S}, \mathbf{r}_0, u)p(\mathbf{r}_0, \mathbf{R}, t - u) du}{p(\mathbf{S}, \mathbf{R}, t)}, \quad (3)$$

where \mathbf{S} and \mathbf{R} are the positions of the source and the receiver, \mathbf{r}_0 is the position of the local velocity variation, and t is the centre of the time interval in the coda where the stretching is evaluated. Here, $p(\mathbf{a}, \mathbf{b}, t)$ is the probability that the wave has travelled from \mathbf{a} to \mathbf{b} during time t . This can be approximated by the intensity of the scattered wave field from \mathbf{a} to \mathbf{b} at time t . Following Planès *et al.* (2014), we use the 3-D radiative transfer solution IRT3D (Paasschens 1997) for isotropic scattering to model the intensity transport of the body waves. With this formulation, we do not consider mode conversions but describe P and S waves as a single effective mode with an effective speed c_E . For a local velocity variation $\frac{dv}{v}$ in an elementary volume ΔV centred on \mathbf{r}_0 , $\varepsilon^{\text{Body}}(\mathbf{r}_0, t)$ for signals emitted in \mathbf{S} and received in \mathbf{R} reads:

$$\varepsilon^{\text{Body}}(\mathbf{r}_0, t) = \frac{K(\mathbf{S}, \mathbf{R}, \mathbf{r}_0, t)}{t} \frac{dv}{v} \Delta V. \quad (4)$$

For more details please refer to Obermann *et al.* (2013b).

3.2.3 Combined sensitivity

We then combine the two sensitivities as described by eq. (2). With a least-squares criterion, we search the partition coefficient α that optimizes the fit of the depth sensitivity from the numerical simulations. In Fig. 4, we show that the modelled combined sensitivities $\varepsilon^{\text{Theo}}$ (dashed red line) fit the observations very well. The broken black line in Fig. 4 indicates the modelled prediction assuming body waves only ($\varepsilon^{\text{Body}}$). While the body waves can explain the sensitivity behaviour at depths greater than 0.5 km, we need the surface wave sensitivity to explain the observed sensitivity at shallower depths. The partition ratio for the displayed example is $\alpha = 0.75$, indicating the dominant importance of surface waves at short lapse times. For very small values of α , the sensitivity would approach the modelled prediction assuming body waves only ($\varepsilon^{\text{Body}}$). Please note that even though we do not explicitly include surface-body wave mode conversions in the 2-D and 3-D kernel formulations, we effectively take into account these conversions as we allow the partition ratio to vary along time in the coda.

3.3 Partition ratio between body- and surface-wave sensitivity in different settings

We now study the evolution of the partition coefficients for different levels of heterogeneity in the models (different ℓ^*) and at different times in the coda. We normalize the time axis by the transport mean free time $t^* = \ell^*/c_E$ and plot the partition coefficients against the dimensionless axis t/t^* (Fig. 5a). We find a universal behaviour of the partition ratio of body and surface wave energy. We observe that the surface waves dominate the depth sensitivity for about eight mean free times, while the body waves dominate the depth sensitivity at later times. In Fig. 5(b), we show for comparison the 2-D case, where the surface waves dominate during six to eight mean free times. We find a very good agreement between the results in 2-D and 3-D, despite the differences in the simulation solvers.

4 LAPSE TIME EVOLUTION OF SENSITIVITY FOR DIFFERENT CONFIGURATIONS OF MEDIUM CHANGES

In this section, we study the imprint of different medium perturbations on the lapse-time behaviour in the coda. We chose two configurations to address the practical issue of determining the origin of the velocity changes detected after large earthquakes. The change could be related to the nonlinear behaviour of shallow unconsolidated materials (sketched as a horizontal layer, Fig. 6a) or the response of the damaged rocks of the fault zone (sketched as a vertical layer, Fig. 6b) and the strain in the bulk.

The distance d between the layer and the receiver array is either $d = 100$ m ($\approx 1/3\lambda$) or $d = 1500$ m ($\approx 5\lambda$). For each case, we determine the resulting apparent velocity changes (ε^{obs}) in overlapping 1 s long time-windows in the coda of the signals recorded along a line of surface receivers. The apparent velocity changes are averaged over the 20 receivers and are shown in Figs 6(a) and (b) below the sketches versus the time in the coda; along with the corresponding correlation coefficients CC (blue for $d = 100$ m, red for $d = 1500$ m).

Surface waves emitted by the source will sample the horizontal perturbation at shallow depth, as they are sensitive to a depth of $\approx 1/3\lambda$ (Fig. 6a). Their contribution is high at early times in the

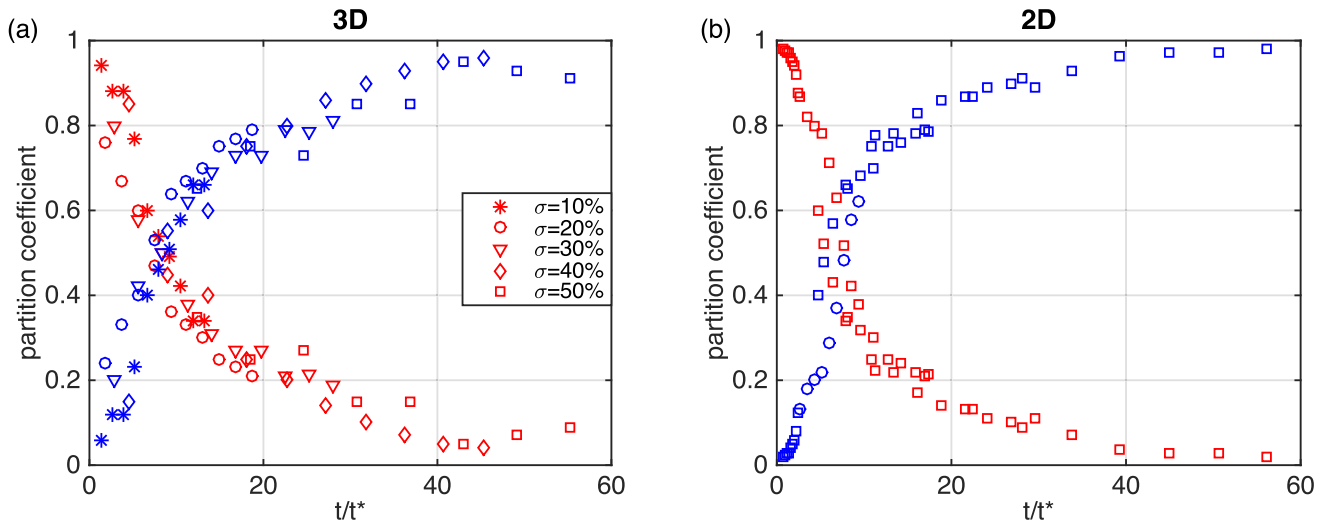


Figure 5. Evolution of the partition coefficients for different degrees of heterogeneity in 3-D (a) and 2-D (b, from Obermann *et al.* (2013b)). The time axis has been normalized by the transport mean free time $t^* = \ell^*/c$. Displayed in red are the partition coefficients α for the surface wave sensitivity, and in blue $1 - \alpha$ for the body wave sensitivity.

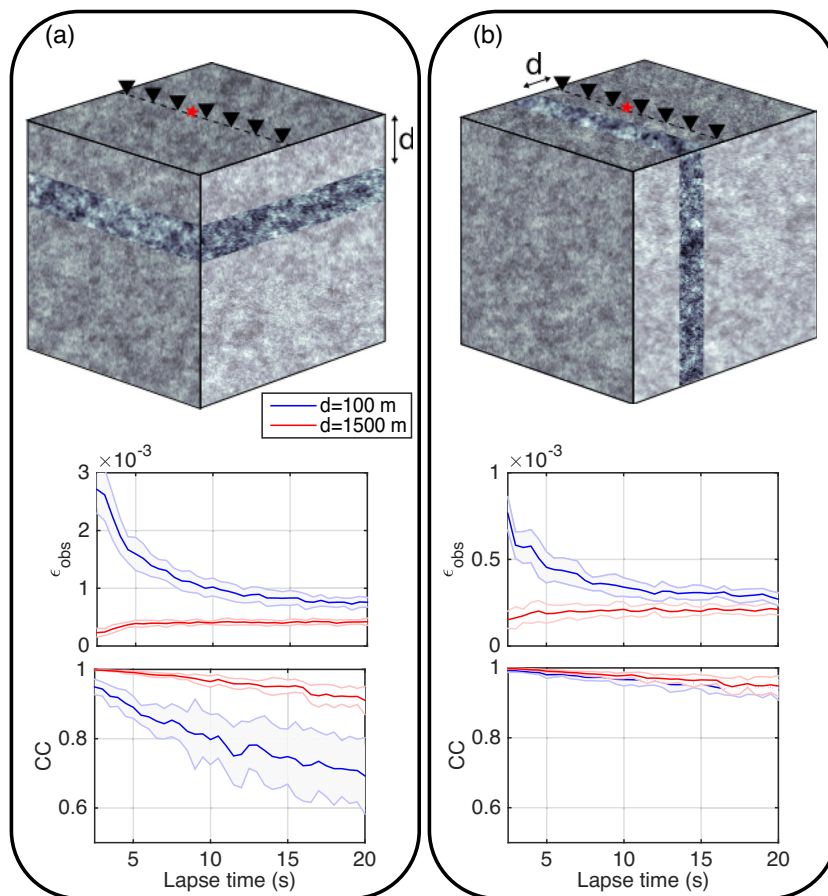


Figure 6. (a) Sketch of a horizontal velocity perturbation at distance d from the receiver array. (b) Sketch of a vertical velocity perturbation at distance d from the receiver array. Below each sketch are the corresponding apparent relative velocity changes ϵ_{obs} versus time in the coda and the respective correlation coefficients CC. The shaded area represents one standard deviation obtained after averaging over 20 receivers. The distance d is either 100 m ($\approx 1/3\lambda$, blue) for a close-by perturbation or 1500 m ($\approx 5\lambda$, red) for a distant medium perturbation.

coda and then continuously decreases at later times. This means that a strong velocity change ϵ_{obs} will be observed already at early lapse times. Towards later lapse times, the partition coefficient of body waves steadily increases. Some of these body waves have also

encountered the shallow perturbation. Thus, a contribution to ϵ_{obs} is still present at later lapse times, although it is much weaker then. Since most surface waves are affected by the shallow perturbed layer starting from zero lapse time, the waveform starts to lose

coherency immediately, and the CC continues to drop with lapse time.

For a horizontally perturbed layer at greater depth, a different lapse time behaviour of ϵ_{obs} is observed. At very early lapse times, the wavefield is still dominated by surface waves. Since their sensitivity does not reach deep enough to be affected by the changed medium, no velocity change is detected. It is only at later time in the coda that an apparent velocity change builds up, as the probability increases that deeper travelling body waves return to the surface, after sensing the perturbation. These body waves have spent on average more time at greater depth, sampling the area densely and hence becoming more sensitive to medium changes. The loss of CC with lapse time is much less severe in this case, as only a small part of the wavefield contributes to the decoherence of the waveform.

For a vertically extended perturbation at close lateral distance to the source and receiver, waves which have travelled a short distance only may have already sampled the perturbation. Thus, at early coda times, a velocity change is observed (Fig. 6b). For later lapse times, there is still a probability that a part of the wavefield has travelled through the perturbation, resulting in an ϵ_{obs} . The main difference between the vertical and horizontal close-by layer is that only the part of the surface wavefield that directly passes through the perturbation cause an apparent velocity change. The sensitivity to a shallow horizontal layer is hence larger than to a vertical one as expected from the presence of surface waves.

In the case of vertical perturbations, the difference in sensitivity kernels for surface and body waves is less relevant. In other words, the contribution of both surface and body waves to the ϵ_{obs} is similar in nature, resulting in a less pronounced difference in lapse-time behaviour between a far and nearby perturbation. However, a difference can still be seen at early times in the coda. For a perturbation at greater horizontal distance, a certain time is needed before scattered waves have propagated far enough to encounter the perturbation and come back to the receiver. Therefore, the sensitivity towards change is slightly lower at early lapse time.

Although the overall behaviour is similar, we notice quantitative differences between vertically and horizontally oriented medium perturbations. The total sensitivity is 3.5 times higher for the shallow horizontal layer (Fig. 6a) than for a single vertical layer located near the receiver line (Fig. 6b).

While a lapse-time analysis offers the possibility to discriminate a change that occurs close to the receiver array from a change that occurs further away, the qualitative sensitivity behaviour of the coda waves is similar for vertical and horizontal perturbations. To determine the geometry of the medium perturbation more detailed analyses are necessary. This could, for instance, be done by studying 2-D surface arrays, as the sensitivity depends on the offset between source and receiver for a vertical layer.

5 CONCLUSIONS

We investigated the sensitivity of coda waves to velocity perturbations localized in slabs of finite thickness in 3-D heterogeneous elastic media. We addressed two problems. First we evaluated the contribution of surface and body wave sensitivity to a change at depth. Second we compared the cases of a perturbation in horizontal and vertical slabs to address, for instance, the origin of the velocity changes detected after large earthquakes.

We ran numerical wavefield simulations in media with different degrees of heterogeneity that contain a thin layer with a slightly perturbed velocity at different depths. For all different model het-

erogeneities, we could relate the depth sensitivity of coda waves to a combination of body- and surface-wave sensitivity. Analogous to the 2-D case, we found a universal behaviour of the partition ratio of body and surface waves versus the normalized lapse-time. With the universal partition ratio we can create 3-D sensitivity kernels as a combination of 2-D and 3-D kernels. Imaging with such 3-D kernels that are critical for depth location, could significantly improve our understanding of the nature of the medium variations revealed by seismic monitoring.

The lapse-time dependence of the relative velocity changes in the coda allows us to discriminate a change that occurs close to the receiver array from a change that occurs at several wavelengths distance. However, the qualitative sensitivity behaviour for vertically and horizontally extended changes is similar, making a discrimination without more detailed 2-D array analysis difficult.

Recently, Margerin *et al.* (2016) pointed out that the anisotropic scattering should be considered properly in the radiative transfer equation for the computation of sensitivity kernels. We remind the linear nature of the perturbative effects considered here that allow for deducing composite models from the simple cases presented. In future works, there is a need to explicitly consider the specific intensity in place of the total intensity [as done in the IRT3D solution by Paasschens (1997)]. The differences are particularly important in cases of strongly anisotropic scattering Margerin *et al.* (2016) and when analysing simultaneously phase delays and waveform decoherence.

ACKNOWLEDGEMENTS

The research leading to these results has received funding from the European Community's Seventh Framework Programme under grant agreement No. 608553 (Project IMAGE) and the Swiss Federal office of Energy with the project GEOBEST. CH acknowledges support from grant HA7019/1-1 by the Emmy-Noether Programme of the German Research Foundation (DFG). AO is grateful for a visiting fellowship from the Center for Advanced Studies (CAS) at the LMU, Munich. The authors also want to thank the Leibniz-Rechenzentrum (LRZ) and Jens Oeser for access and support in using the SUPERMUC system at the LRZ. AO thanks Stijn Vantieghem and Manuel Chaljub for help with the SPECFEM3D codes. The authors wish to thank Nori Nakata and an anonymous reviewer for comments which helped to significantly improve the manuscript.

REFERENCES

- Aki, K., 1969. Analysis of seismic coda of local earthquake as scattered waves, *J. geophys. Res.*, **74**(2), 615–631.
- Aki, K. & Richards, P., 1980. *Quantitative Seismology: Theory and Methods*, vol. I, WH Freeman & Co.
- Brenguier, F., Shapiro, N.M., Campillo, M., Ferrazzini, V., Duputel, Z., Coutant, O. & Nercessian, A., 2008. Towards forecasting volcanic eruptions using seismic noise, *Nat. Geosci.*, **1**, 126–130.
- Chaput, J., Campillo, M., Aster, R., Roux, P., Kyle, P., Knox, H. & Czoski, P., 2015. Multiple scattering from icequakes at Erebus volcano, Antarctica: implications for imaging at glaciated volcanoes, *J. geophys. Res.*, **120**(2), 1129–1141.
- Chen, J.H., Froment, B., Liu, Q.Y. & Campillo, M., 2010. Distribution of seismic wave speed changes associated with the 12 May 2008 Mw 7.9 Wenchuan earthquake, *Geophys. Res. Lett.*, **37**, L18302, doi:10.1029/2010GL044582.

- Froment, B., Campillo, M., Chen, J.H. & Liu, Q.Y., 2013. Deformation at depth associated with the May 12, 2008 Mw 7.9 Wenchuan earthquake from seismic ambient noise monitoring, *Geophys. Res. Lett.*, **40**, 78–82.
- Hadziioannou, C., Larose, E., Coutant, O., Roux, P. & Campillo, M., 2009. Stability of monitoring weak changes in multiply scattering media with ambient noise correlation: laboratory experiments, *J. acoust. Soc. Am.*, **125**(6), 3688–3695.
- Hennino, R., Tregoures, N., Shapiro, N.M., Margerin, L., Campillo, M., van Tiggelen, B.A. & Weaver, R.L., 2001. Observation of equipartition of seismic waves, *Phys. Rev. Lett.*, **86**(15), 3447–3450.
- Hillers, G., Husen, S., Obermann, A., Planès, T., Campillo, M. & Larose, E., 2015. Noise-based monitoring and imaging of aseismic transient deformation induced by the 2006 Basel reservoir stimulation, *Geophysics*, **80**(4), KS51–KS68.
- Hobiger, M., Wegler, U., Shiomi, K. & Nakahara, H., 2012. Coseismic and postseismic elastic wave velocity variations caused by the 2008 Iwate-Miyagi Nairiku earthquake, Japan, *J. geophys. Res.*, **117**(B9), doi:10.1029/2012JB009402.
- Kanu, C. & Snieder, R., 2015. Numerical computation of the sensitivity kernel for monitoring weak changes with multiply scattered acoustic waves, *Geophys. J. Int.*, **203**(3), 1923–1936.
- Komatitsch, D. & Tromp, J., 2002. Spectral-element simulations of global seismic wave propagation – II. Three-dimensional models, oceans, rotation and self-gravitation, *Geophys. J. Int.*, **150**(1), 303–318.
- Larose, E., Planès, T., Rossetto, V. & Margerin, L., 2010. Locating a small change in a multiple scattering environment, *Appl. Phys. Lett.*, **96**, 204101, doi:10.1063/1.3431269.
- Larose, E., Obermann, A., Digulescu, A., Planès, T., Chaix, J.F., Mazerolle, F. & Moreau, G., 2015. Locating and characterizing a crack in concrete with LOCADIFF: a four-point bending test, *J. acoust. Soc. Am.*, **138**(1), 232–241.
- Lobkis, O.I. & Weaver, R.L., 2003. Coda-wave interferometry in finite solids: recovery of P-to-S conversion rates in an elastodynamic billiard, *Phys. Rev. Lett.*, **90**(25), doi:10.1103/PhysRevLett.90.254302.
- Margerin, L., Campillo, M., Shapiro, N.M. & van Tiggelen, B., 1999. Residence time of diffuse waves in the crust and the physical interpretation of coda Q. Application to seismograms recorded in Mexico, *Geophys. J. Int.*, **138**, 343–352.
- Margerin, L., Campillo, M., Van Tiggelen, B. & Hennino, R., 2009. Energy partition of seismic coda waves in layered media: theory and application to pinyon flats observatory, *Geophys. J. Int.*, **177**(2), 571–585.
- Margerin, L., Planès, T., Mayor, J. & Calvet, M., 2016. Sensitivity kernels for coda-wave interferometry and scattering tomography: theory and numerical evaluation in two-dimensional anisotropically scattering media, *Geophys. J. Int.*, **204**(1), 650–666.
- Nakahara, H. & Carcolé, E., 2010. Maximum-likelihood method for estimating coda Q and the Nakagami-m parameter, *Bull. seism. Soc. Am.*, **100**(6), 3174–3182.
- Nakata, N. & Beroza, G.C., 2015. Stochastic characterization of mesoscale seismic velocity heterogeneity in Long Beach, California, *Geophys. J. Int.*, **203**(3), 2049–2054.
- Obermann, A., Planès, T., Larose, E. & Campillo, M., 2013a. Imaging pre- and co-eruptive structural and mechanical changes on a volcano with ambient seismic noise, *J. Geophys. Res.*, **118**(12), 6285–6294.
- Obermann, A., Planès, T., Larose, E., Sens-Schönfelder, C. & Campillo, M., 2013b. Depth sensitivity of seismic coda waves to velocity perturbations in an elastic heterogeneous medium, *Geophys. J. Int.*, **194**(1), 372–382.
- Obermann, A., Larose, E., Margerin, L. & Rossetto, V., 2014. Measuring the scattering mean free path of Rayleigh waves on a volcano from spatial phase decoherence, *Geophys. J. Int.*, **197**, 435–442.
- Obermann, A., Kraft, T., Larose, E. & Wiemer, S., 2015. Potential of ambient seismic noise techniques to monitor the St. Gallen geothermal site (Switzerland), *J. Geophys. Res.*, **120**(6), 4301–4316.
- Paasschens, J.C.J., 1997. Solution of the time-dependent Boltzmann equation, *Phys. Rev. E*, **56**(1), 1135, doi:10.1103/PhysRevE.56.1135.
- Pacheco, C. & Snieder, R., 2005. Time-lapse travel time change of multiply scattered acoustic waves, *J. acoust. Soc. Am.*, **118**, 1300–1310.
- Peter, D. et al., 2011. Forward and adjoint simulations of seismic wave propagation on fully unstructured hexahedral meshes, *Geophys. J. Int.*, **186**(2), 721–739.
- Planès, T., Larose, E., Margerin, L., Rossetto, V. & Sens-Schönfelder, C., 2014. Decorrelation and phase-shift of coda waves induced by local changes: multiple scattering approach and numerical validation, *Waves Random Complex Media*, **2**(24), 1–27.
- Planès, T., Larose, E., Rossetto, V. & Margerin, L., 2015. Imaging multiple local changes in heterogeneous media with diffuse waves, *J. acoust. Soc. Am.*, **2**(137), 660–667.
- Poupinet, G., Ellsworth, W.L. & Frechet, J., 1984. Monitoring velocity variations in the crust using earthquake doublets: an application to the Calaveras fault, California, *J. geophys. Res.*, **89**(B7), 5719–5731.
- Poupinet, G., Ratdomopurbo, A. & Coutant, O., 1996. On the use of earthquake multiplets to study fractures and the temporal evolution of an active volcano, *Ann. Geophys.*, **39**, 253–264.
- Reasenber, P. & Aki, K., 1974. A precise, continuous measurement of seismic velocity for monitoring in situ stress, *J. Geophys. Res.*, **79**(2), 399–406.
- Rivet, D., Campillo, M., Shapiro, N.M., Cruz-Atienza, V., Radiguet, M., Cotte, N. & Kostoglodov, V., 2011. Seismic evidence of nonlinear crustal deformation during a large slow slip event in Mexico, *Geophys. Res. Lett.*, **38**, L08308, doi:10.1029/2011GL047151.
- Salvermoser, J., Hadziioannou, C. & Stähler, S.C., 2015. Structural monitoring of a highway bridge using passive noise recordings from street traffic, *J. acoust. Soc. Am.*, **138**(6), 3864–3872.
- Sato, H., Fehler, M. & Wu, R., 2002. Scattering and attenuation of seismic waves in the lithosphere, *Int. Geophys.*, **81**(A), 195–208.
- Sens-Schönfelder, C. & Wegler, U., 2006. Passive image interferometry and seasonal variations of seismic velocities at Merapi Volcano, Indonesia, *Geophys. Res. Lett.*, **33**(21), L21302, doi:10.1029/2006GL027797.
- Sens-Schönfelder, C. & Wegler, U., 2011. Passive image interferometry for monitoring crustal changes with ambient seismic noise, *C. R. Geosci.*, **343**(8), 639–651.
- Shapiro, N.M., Campillo, M., Margerin, L., Singh, S.K., Kostoglodov, V. & Pachero, J., 2000. The energy partitioning and the diffuse character of the seismic coda, *Bull. seism. Soc. Am.*, **90**, 655–665.
- Snieder, R., Grêt, A., Douma, H. & Scales, J., 2002. Coda wave interferometry for estimating nonlinear behavior in seismic velocity, *Science*, **295**(5563), 2253–2255.
- Trégoures, N., Hennino, R., Lacombe, C., Shapiro, N., Margerin, L., Campillo, M. & van Tiggelen, B., 2002. Multiple scattering of seismic waves, *Ultrasonics*, **40**(1), 269–274.
- Weaver, R.L., 1982. On diffuse waves in solid media, *J. acoust. Soc. Am.*, **71**, 1608–1609.
- Weaver, R.L., 1985. Diffuse elastic waves at a free surface, *J. acoust. Soc. Am.*, **78**, 131–136.
- Zhang, Y., Planès, T., Larose, E., Obermann, A., Rospars, C. & Moreau, G., 2016. Diffuse ultrasound monitoring of stress and damage development on a 15-ton concrete beam, *J. acoust. Soc. Am.*, **139**(4), 1691–1701.

SUPPORTING INFORMATION

Additional Supporting Information may be found in the online version of this paper:

Figure S1. Reflections as observed on the vertical and horizontal components in a homogeneous half-space ($x, y = 10$ km, $z = 6$ km). The source is located at $x = 5$ km, $y = 3$ km, $z = 1$ km. Thirteen receivers are arranged with 500 m spacing along a line at $y = 3$ km, $z = 1$ km. Potential absorbing boundary reflections are indicated with red dots. (<http://gji.oxfordjournals.org/lookup/suppl/doi:10.1093/gji/ggw264/-/DC1>)

Please note: Oxford University Press is not responsible for the content or functionality of any supporting materials supplied by the authors. Any queries (other than missing material) should be directed to the corresponding author for the paper.